

Magnetomechanical Accelerometer Based on Magnetic Tunnel Junctions

Andrea Meo¹,^{*} Francesca Garescì², Victor Lopez-Dominguez,^{3,4} Davi Rodrigues¹,^{*} Eleonora Raimondo⁵, Vito Puliafito,¹ Pedram Khalili Amiri^{4,*}, Mario Carpentieri^{1,†} and Giovanni Finocchio^{5,‡}


¹*Department of Electrical and Information Engineering, Politecnico di Bari, Bari 70125, Italy*

²*Department of Engineering, University of Messina, Messina I-98166, Italy*

³*Institute of Advanced Materials (INAM), Universitat Jaume I, Castellon 12006, Spain*

⁴*Department of Electrical and Computer Engineering, Northwestern University, 2145 Sheridan Road, Evanston 60208, Illinois, USA*

⁵*Department of Mathematical and Computer Sciences, Physical Sciences and Earth Sciences, University of Messina, Messina I-98166, Italy*

 (Received 4 April 2023; revised 6 July 2023; accepted 7 August 2023; published 5 September 2023)

Accelerometers have widespread applications and are an essential component in many areas, such as automotive, consumer electronics, and industrial applications. Most commercial accelerometers are based on a microelectromechanical system (MEMS) that is limited in downscaling and power consumption. Spintronics-based accelerometers are proposed as alternatives; however, current proposals suffer from design limitations that result in reliability issues and high cost. Here, we propose spintronic accelerometers with magnetic tunnel junctions (MTJs) as building blocks, which map accelerations into a measurable voltage across the MTJ terminals. The device exploits elastic and dipolar coupling as a sensing mechanism and the spintronic diode effect for the direct readout of acceleration. The proposed technology represents a potentially competitive and scalable solution to current capacitive MEMS-based approaches that could lead to a step forward in many of the commercial applications.

DOI: [10.1103/PhysRevApplied.20.034003](https://doi.org/10.1103/PhysRevApplied.20.034003)

I. INTRODUCTION

Accelerometers are an essential component in many applications, such as automotive [1], consumer electronics [2], seismic monitoring [3], human-computer interaction [4], and Industry 4.0 [5], with the emerging internet of things [6], internet of everything [7], and digital twins [8]. Most commercial accelerometers are based on microelectromechanical systems (MEMSs) built with heterogeneous integration [9–11], and among them, capacitive MEMS-based accelerometers are the most common. They exploit the change of capacitance between a fixed electrode and a movable one attached to a spring that behaves as a proof mass. The change in capacitance relates to the acceleration acting on the device, and it allows the measurement of acceleration [3,12]. The main limitations of MEMS-based accelerometers are the difficulty of downscaling, lack of electromagnetic radiation hardness, and high-power consumption, as it is required to charge the capacitive plates [3,13].

Spintronics is now an active area of research, development, and applications [14,15]. The compatibility with complementary metal oxide semiconductor (CMOS) manufacturing processes [16–19], as well as recent advancements in material and device fabrication, have been driving the development of the key building blocks of spintronics, i.e., magnetic tunnel junctions (MTJs) [16,17,20], to be ready for exploitation in commercial applications, such as magnetic sensors [17,21,22], memories [15,23], oscillators [24], and others [16,17,20]. The active part of the MTJ is composed of two ferromagnetic layers, pinned and free layers, separated by a thin isolating material. The resistance of an MTJ depends on the relative orientation of the free-layer magnetization with respect to the fixed-layer one.

Some spintronics-based accelerometers have been proposed in recent years [25–29]. Such proposals rely on mechanical stresses acting on the MTJ device itself, be it a moving component of the MTJ [25,29] or a cantilever closing into the MTJ [26,27]. However, these approaches can result in a potential rapid degradation of the magnetic properties and tunneling magnetoresistance of the MTJ because of their complex structure, causing reliability issues as well as inducing structural damage. Moreover, the fabrication

^{*}pedram@northwestern.edu

[†]mario.carpentieri@poliba.it

[‡]gfinocchio@unime.it

of these devices would require the development of *ad hoc* processes and techniques not compatible with the current processes implemented for MTJs, resulting in expensive and complex products.

Here, we propose a spintronic MEMS accelerometer designed by coupling micromagnetic simulations and elastic dynamics, drawing inspiration from capacitive MEMS-based accelerometers. The device concept comprises two MTJs working as spin-torque nano-oscillators (STNOs) that are magnetically and elastically coupled. One MTJ is realized on top of a fixed substrate (fixed MTJ), while the other is deposited on top of a substrate that is free to move (free MTJ) but elastically connected to the fixed one. To work as a MEMS, the two MTJs have to be magnetically coupled throughout the whole range of displacements that the substrates can reach. The spintronic diode effect across the fixed MTJ is used as a readout mechanism [20,30]. We first design the fixed MTJ, considering experimentally measured physical parameters, where the magnetization dynamics is characterized by the excitation of a uniform mode. The free MTJ is designed in such a way that the rectified voltage in the fixed MTJ changes linearly as a function of the distance between the free and fixed MTJs. Variations of the rectified voltage can be linked directly to the external acceleration acting on the free MTJ because the magnetization dynamics is much faster than the elastic one. With experimentally achievable parameters, we predict rectification voltages on the order of tens of microvolts. Our results show that the spintronic MEMS devices proposed here can be potentially competitive candidates to replace current capacitive MEMS-based accelerometers owing to their compactness, CMOS compatibility, and high sensitivity.

The paper is organized as follows. Section II presents the working principle of the proposed spintronic MEMS accelerometer. The device design and the numerical modeling approach utilized in this study are presented and discussed in Sec. III. The approach is validated by characterizing the fixed MTJ in Sec. IV, while the two-MTJ system is modeled and analyzed in Sec. V. Section VI is dedicated to simulations of the behavior of a spintronic MEMS device in a potential operational environment. Finally, Sec. VII summarizes the main conclusions of this study.

II. WORKING PRINCIPLE

Figure 1(a) shows the established design of a capacitive MEMS-based accelerometer. A proof mass and the electrodes attached to it are displaced with respect to fixed electrodes upon application of an external acceleration, and the change in differential capacitance [$C_1 - C_2$ in Fig. 1(a)] is used to estimate the acceleration. An MTJ-based accelerometer can be designed in different ways. In particular, a concept similar to the capacitive MEMS-based

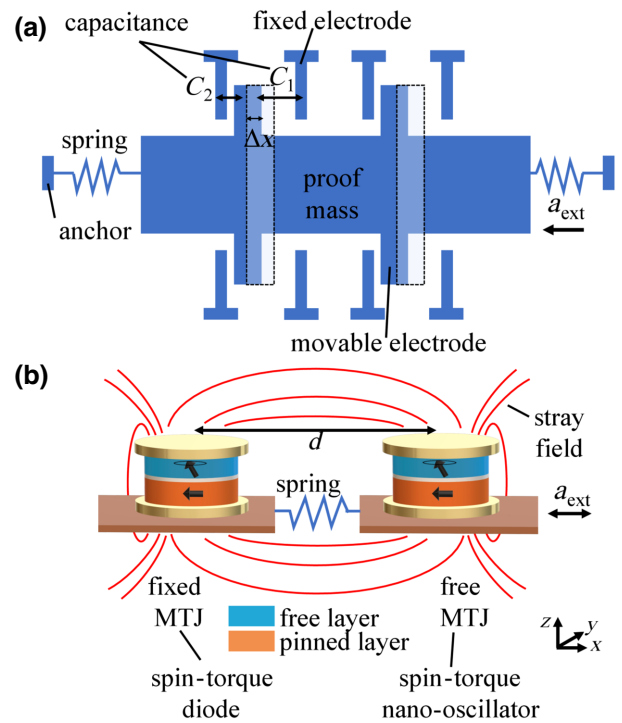


FIG. 1. (a) Schematic description of the working principle of a capacitive MEMS accelerometer composed of fixed electrodes and a movable structure with capacitive “fingers” defining a proof mass connected to anchors via springs. Each finger electrode, i , is characterized by a capacitance, $C_{i=1,2,\dots}$. Δx is the displacement of the proof mass from the equilibrium position (shaded area) induced by the action of an external acceleration, a_{ext} . (b) Schematic description of the proposed spintronic MEMS accelerometers. System of two MTJs, composed of a free layer and a pinned layer, is coupled via a dipolar field (red lines) and elastically via the substrates. Free MTJ, acting as a spin-torque nano-oscillator, is displaced from its equilibrium position (shaded area) of Δx when an external acceleration, a_{ext} , is applied, resulting in a change in the MTJ center-to-center distance (d), and thus, in the stray-field distribution. Readout mechanism is based on the spintronic diode effect on the fixed MTJ that acts as a spin-torque diode. Cartesian coordinate system used in this paper is also included.

accelerometer can be exploited by considering a pair of MTJs placed on top of two substrates connected via an elastic element, as shown in Fig. 1(b). One substrate is fixed, while the other substrate is free to move along a fixed direction in response to an external excitation, and we refer to the MTJs mounted on top of each substrate as fixed MTJ and free MTJ, respectively. In this design, the two MTJs are coupled elastically through the substrate and magnetically via their dipolar interactions. In the presence of an acceleration, the relative distance between the MTJs changes and is translated into a change in the stray-field configuration between them (red lines). The proposed solution relies on the spintronic diode effect [20,31]. The two

MTJs are in the self-oscillation regime driven by a constant applied current, both working as the STNO [32,33]. An ac current is applied to the fixed MTJ to precisely control the oscillation frequency, thanks to the injection-locking phenomenon. The spintronic diode effect measurable in the injection-locked states exhibits very high sensitivity enhanced by the dc bias current [20,31,34]. Therefore, the fixed MTJ works as an active spin-torque diode. In addition, the system is designed in such a way that the oscillatory dynamics of the two MTJs is mutually synchronized via the dynamic stray field. In this configuration, the rectified voltage across the fixed MTJ depends on the distance between the two MTJs. An alternative solution, where a coil is placed in between the MTJs, to perform the readout is presented in Note S1 of the Supplemental Material [32]. However, the simpler and smaller design, together with the use of the spintronic diode effect, make the solution of Fig. 1(b) more appealing. Moreover, the spintronic accelerometer proposed here senses the acceleration directly as voltage variation across the fixed MTJ. Once amplified by an external circuit, the signal can be used for the evaluation of the acceleration directly, in contrast to state-of-the-art integrable MEMS devices, where a circuit to convert the capacitance variation into an output voltage and then an amplification are needed [13,33,34].

III. MODEL

The magnetic behavior of the spintronic MEMS accelerometer is simulated by numerically integrating two coupled Landau-Lifshitz-Gilbert-Slonczewski equations for the free and fixed MTJs [35–37], whereas the elastic dynamics is described in Eq. (2):

$$\begin{aligned}
\frac{d\mathbf{m}_1}{d\tau} &= -\frac{1}{1+\alpha^2}(\mathbf{m}_1 \times \mathbf{h}_{\text{eff},1}) \\
&\quad -\frac{\alpha}{1+\alpha^2}[\mathbf{m}_1 \times (\mathbf{m}_1 \times \mathbf{h}_{\text{eff},1})] \\
&\quad +\frac{\sigma_1 I_1 g_T}{1+\alpha^2}[\mathbf{m}_1 \times (\mathbf{m}_1 \times \mathbf{m}_p) - q(\mathbf{m}_1 \times \mathbf{m}_p)], \\
\frac{d\mathbf{m}_2}{d\tau} &= -\frac{1}{1+\alpha^2}(\mathbf{m}_2 \times \mathbf{h}_{\text{eff},2}) \\
&\quad -\frac{\alpha}{1+\alpha^2}[\mathbf{m}_2 \times (\mathbf{m}_2 \times \mathbf{h}_{\text{eff},2})] \\
&\quad +\frac{\sigma_2 I_2 g_T}{1+\alpha^2}[\mathbf{m}_2 \times (\mathbf{m}_2 \times \mathbf{m}_p) - q(\mathbf{m}_2 \times \mathbf{m}_p)].
\end{aligned} \tag{1}$$

Here, α is the Gilbert damping coefficient, $\mathbf{m}_i = \mathbf{M}_i/M_{s,i}$ with $i = 1, 2$ is the normalized magnetization vector of the free layer (FL) of MTJ i (1 corresponds to a fixed MTJ; 2 corresponds to a free MTJ) of saturation magnetization $M_{s,i}$ and volume $V_{\text{FL},i}$, and $\tau = \gamma_0 M_{s,i} t$ is the dimensionless time with γ_0 being the gyromagnetic ratio

and t the time. The effective field acting on MTJ i ($\mathbf{h}_{\text{eff},i}$) includes the contributions from exchange ($\mathbf{h}_{\text{ex},i}$), uniaxial anisotropy ($\mathbf{h}_{u,i}$), the demagnetization field ($\mathbf{h}_{\text{demag},i}$), and the dipolar field ($\mathbf{h}_{\text{dip},j \rightarrow i}$) acting on MTJ i due to MTJ j . The latter is the coupling mechanism of the two MTJs in the proposed device. The strength of the spin-transfer torque is given by the term $I_i \sigma_i g_T$, where I_i is the injected current in MTJ i comprising both dc and ac components, $I_i = I_{\text{dc},i} + I_{\text{ac},i} \sin(2\pi f_{\text{ac}} + \varphi_{\text{ac}})$; $\sigma_i = g\mu_B / (e\gamma_0 M_{s,i} V_{\text{FL},i})$; and $g_T = 2\eta / (1 + \eta^2 \cos \vartheta)$ is the polarization function that depends on the angle formed between \mathbf{m}_i and the pinned-layer (\mathbf{m}_p) magnetization [38,39]. We observe that we consider, without loss of generality, that both MTJs have the same g_T and \mathbf{m}_p [$\mathbf{m}_p = -\hat{x} = (-1, 0, 0)$]. Micromagnetic calculations are performed by means of the micromagnetic solver PETASPIN utilizing an adaptive semi-implicit scheme [37,39]. In macrospin simulations, we exploit the uniform magnetization hypothesis to compute $\mathbf{h}_{\text{demag},i}$ as $\mathbf{h}_{\text{demag},i} = -\bar{N}\mathbf{m}_i$ and $\mathbf{h}_{\text{dip},j \rightarrow i}$ as $\mathbf{h}_{\text{dip},j \rightarrow i} = (\mu_0/4\pi r_{ij}^3)[3\hat{\mathbf{r}}_{ij}(\mathbf{m}_j \cdot \hat{\mathbf{r}}_{ij}) - \mathbf{m}_j] = \bar{D} \cdot \mathbf{m}_j$ via dipolar approximation, where \bar{N} is a diagonal matrix with the demagnetization factors as elements, $\hat{\mathbf{r}}_{ij}$ is the unit vector of magnitude r_{ij} of the distance between MTJ i and j , and \bar{D} is the position-dependent dipole matrix. All simulations are performed at zero temperature.

The spintronic MEMS accelerometer employs hybrid MTJs with an out-of-plane FL and in-plane PL patterned into pillars of an elliptical cross section of dimensions $150 \times 70 \text{ nm}^2$, designed according to previous schemes that optimize the rectification response of active spintronic diodes driven by injection locking at zero bias field [40]. A sketch of the MTJs is also shown in Fig. 1(b). The FL is a 1.6-nm-thick layer of $\text{Co}_{20}\text{Fe}_{60}\text{B}_{20}$, whereas the PL can be realized with a thicker ferromagnet or a synthetic antiferromagnet (SAF) exchange biased to an antiferromagnet. The MTJ's magnetic parameters are saturation magnetization, $M_s = 0.95 \text{ MJ}/(\text{m}^3)$; perpendicular magnetic anisotropy, $K_u = 0.545 \text{ MJ}/\text{m}^3$; exchange stiffness, $A_{\text{ex}} = 20 \text{ pJ}/\text{m}$; Gilbert damping, $\alpha = 0.02$; polarization efficiency, $\eta = 0.66$; and a fieldlike torque that is 10% of the damping like torque, $q = 0.1$ [35,41]. The nominal electrical resistances associated with the parallel (R_p) and antiparallel (R_{AP}) configurations of magnetization are 640 and 1200 Ω , respectively [40]. Such MTJs have already been extensively studied experimentally and modeled by micromagnetic simulations [40,41].

To describe the mechanical dynamics of the MTJs, we exploit the fact that the device is designed to have the motion constrained along a fixed direction and that the timescales involved in elastic and magnetic processes are different. These allow us to restrict the dynamics to one dimension and to approximate the MTJ as a point-like object, the position of which is given by its center of mass. Then, the elastic dynamics of the free MTJ

can be described as a one-dimensional driven damped spring-mass harmonic oscillator, governed by

$$m_{\text{tot}} \frac{d^2 u_{\text{MTJ}}}{dt^2} = -b \frac{du_{\text{MTJ}}}{dt} - k_{\text{el}} u_{\text{MTJ}} - F_{\text{mag}} + F_{\text{ext}}. \quad (2)$$

The forces are applied to the center of mass of the free MTJs and the free-MTJ displacement (u_{MTJ}) is along the direction connecting the two MTJs; m_{tot} is the total mass of the accelerometer system. The first term on the right-hand side of the equation is the linear viscous damping with viscous damping coefficient b , the second is the harmonic contribution with elastic constant k_{el} and resonance frequency $\omega_0^2 = k_{\text{el}}/m_{\text{tot}}$, the third one is the magnetic interaction between the MTJs, and $F_{\text{ext}} = m_{\text{tot}} a_{\text{ext}}(t)$ is the driving external force acting on the device with external acceleration $a_{\text{ext}}(t)$. To calculate F_{mag} in this one-dimensional system, we exploit the dipole approximation and the current-loop model [42]. This allows us to express the force acting on the magnetization of the FL of MTJ i due to the stray field from MTJ j ($\mathbf{h}_{\text{dip},j \rightarrow i}$) as $F_{\text{mag}} = \nabla(\boldsymbol{\mu}_i \cdot \mathbf{h}_{\text{dip},i \rightarrow j})$, where $\boldsymbol{\mu}_i = \mathbf{m}_i M_s V_{\text{FL}}$.

IV. DESIGN OF THE FIXED MTJ

A. Magnetization dynamics of the fixed MTJ

Since the MTJ working as an STNO is the main building block of the proposed device, we initially characterize its magnetization dynamics as a function of the dc current, I_{dc} . We perform micromagnetic simulations and verify the uniform nature of the magnetization dynamics, which is a necessary condition to satisfy to apply a macrospin approximation. These are presented and discussed in Note S2 of the Supplemental Material [32]. Figure 2(a) shows the frequency, f , and power, p (dimensionless unit), of the fixed MTJ as a function of the dc current. These data show the working region of the MTJ as an STNO; the dynamic response is characterized by a negative nonlinear frequency shift, $N/2\pi = df/dp$, around -0.75 GHz and a threshold current of -0.065 mA [43]. Once we identify the dynamic properties of the STNO, we evaluate the rectification voltage in the presence of an ac current, $I_{\text{ac}} = 50$ μA , with frequency $f_{\text{ac}} = 0.5$ GHz. The frequency is chosen to be close enough to the oscillation frequency of the oscillator to achieve injection locking and then an enhanced diode effect. Figure 2(b) shows the rectified voltage, V_{dc} , as a function of I_{dc} . The rectification voltage can be expressed analytically as

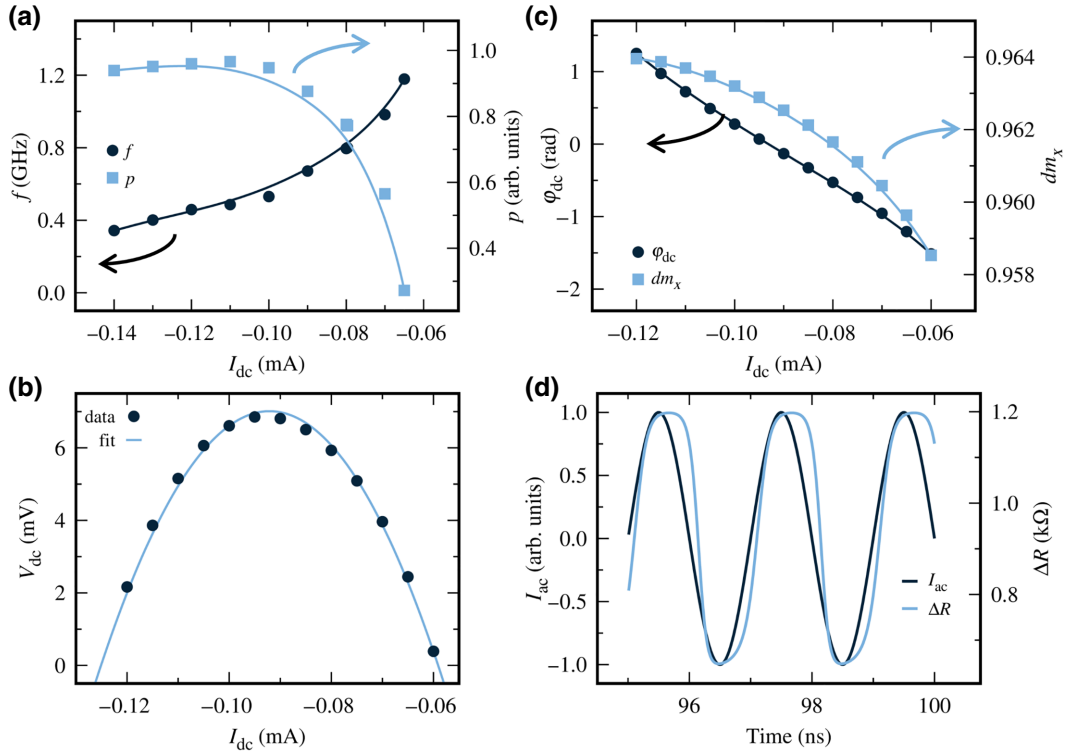


FIG. 2. (a) Oscillation frequency (f) and power (p) of the x component of FL magnetization as a function of applied dc current (I_{dc}); lines are guides to the eye. (b) Rectification voltage (V_{dc}) as a function of I_{dc} (symbols) for $I_{\text{ac}} = 50$ μA and $f_{\text{ac}} = 0.5$ GHz, and the fit (solid line) according to $V_{\text{dc}} = (R_{\text{AP}} - R_{\text{P}})\sqrt{p}/4 I_{\text{ac,max}} \cos[\varphi_{\text{dc}}(I_{\text{dc}})]$. (c) Intrinsic phase shift (φ_{dc}) and amplitude of the x component of magnetization (dm_x) as a function of I_{dc} for a fixed ac current, $I_{\text{ac}} = 50$ μA , at $f_{\text{ac}} = 0.5$ GHz. Lines are guides to the eye. (d) Comparison of time traces of the input current, I_{ac} , and oscillating magnetoresistance (ΔR) for $I_{\text{dc}} = -0.09$ mA, $I_{\text{ac}} = 50$ μA , and $f_{\text{ac}} = 0.5$ GHz.

$V_{dc} = (R_{AP} - R_P)\sqrt{p}/4 I_{ac} \cos[\varphi_{dc}(I_{dc})]$ following Ref. [41]. The maximum $V_{dc}(V_{dc,max})$ is obtained for $\varphi_{dc}(I_{dc}) = 0$. By fitting the quadratic expression of V_{dc} as a function of I_{dc} [solid line in Fig. 2(b)], we extract the dc current that gives $V_{dc,max}$ to be $I_{dc} = -0.09$ mA. Similar qualitative results are observed for $I_{ac} = 25 - 75$ μ A. The validity of the V_{dc} expression is checked with numerical calculations of the oscillator power, p ($\sqrt{p} = dm_x$), and the intrinsic phase shift (φ_{dc}) between the ac current and the oscillating magnetization as a function of I_{dc} , as summarized in Fig. 2(c). Here, the linear dependence of φ_{dc} and weak dependence of dm_x (dm_x variation is less than 1%) can be clearly observed, as expected for an STNO with a large nonlinear frequency shift [43]. Figure 2(d) shows the time traces of the input ac signal and oscillating MTJ magnetoresistance (ΔR) for $I_{dc} = -0.09$ mA. ΔR is computed by considering the following expression: $\Delta R^{-1} = ((R_P^{-1} + R_{AP}^{-1})/2) + ((R_P^{-1} - R_{AP}^{-1})/2) \cos(\beta)$ [40], where β is the angle between FL magnetization \mathbf{m} and \mathbf{m}_p . We point out that, since the polarizer is magnetized along the x direction, the oscillations in ΔR are due to dm_x . For this reason, $\varphi_{dc}(I_{dc})$ of ΔR is the same as that of dm_x . These results agree with previous micromagnetic simulations and experimental reports [40,41] and represent the fundamental basis of our system.

V. MUTUAL SYNCHRONIZATION OF THE FREE AND FIXED MTJs

Once the single STNO is characterized, as the first step towards modeling the accelerometer device, we study the dynamics of the synchronized state of the two MTJs at different distances [d is the center-to-center distance, see Fig. 1(b)]. We set the fixed MTJ into the injection-locked state upon application of ac ($I_{ac,1}$) and dc ($I_{dc,1}$) currents. The free MTJ is then biased with a second dc current ($I_{dc,2}$), which also drives self-oscillations. The two MTJs are coupled via the stray field generated by the two free layers (we consider the pinned layer as an exchange-biased SAF, which generates a reduced-bias dipolar field). To compute the stray field, we apply the dipole approximation, and we consider $d > 350$ nm. At each position, we compute the position-dependent dipole matrix (\vec{D}) and calculate its product with the other MTJ magnetization vector \mathbf{m} . When the two MTJs are far apart, the magnetic interaction is negligible, and their magnetization dynamics are independent. As the MTJs get closer, the dipolar interaction couples the two MTJ dynamics, leading to mutual synchronization [44]. We wish to stress that finding such conditions is crucial for the operation of the spintronic MEMS accelerometer. Based on the characterization of the single STNO, to set the injection locking in the fixed MTJ, we apply $I_{dc,1} = -0.09$ mA, $I_{ac,1} = 50$ μ A, and $f_{ac,1} = 0.5$ GHz. Then, we perform simulations as a function of the center-to-center distance between the MTJs

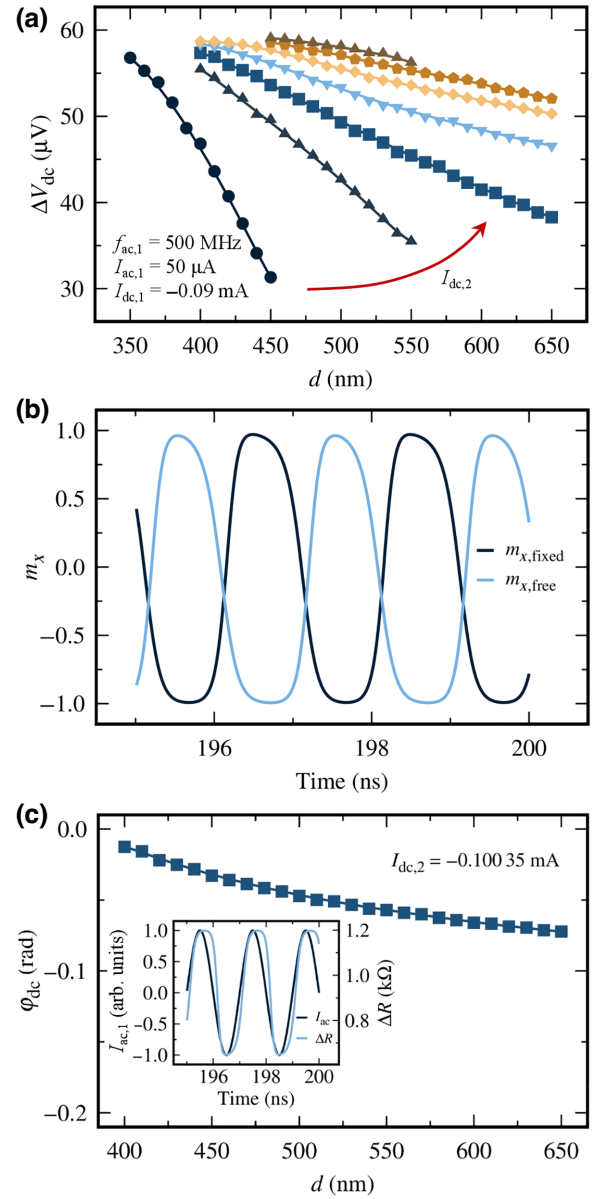


FIG. 3. (a) Rectification voltage, ΔV_{dc} , as a function of the distance between the two MTJs for different dc currents injected into the free MTJ, $I_{dc,2}$ (black dots, -0.099 mA; upwards dark-blue triangles, -0.1 mA; navy-blue squares, -0.10035 mA; downwards light-blue triangles, -0.1008 mA; yellow diamonds, -0.10135 mA; light-brown pentagons, 0.10225 mA; upward dark-brown triangles, 0.10225 mA). (b) Plot of fixed- and free-MTJ m_x components at a distance $d = 450$ nm for $I_{dc,2} = -0.10035$ mA. (c) Intrinsic phase shift (φ_{dc}) as a function of d for $I_{dc,2} = -0.10035$ mA. Inset shows the time traces of the input ac signal, $I_{ac,1}$, and magnetoresistance, ΔR , for $I_{dc,2} = -0.10035$ mA and distance $d = 450$ nm.

(d), as highlighted in Fig. 1(b), by varying $I_{dc,2}$ for values around $I_{dc,1}$. The rectification voltage ($V_{dc,1}^0$) of the fixed MTJ when it is isolated is used as a reference for the calibration of the system. Hence, the rectification voltage

can be expressed as $\Delta V_{\text{dc}} = V_{\text{dc},1} - V_{\text{dc},1}^0$, where $V_{\text{dc},1}$ is the rectification voltage measured across the fixed MTJ when the two MTJs are coupled. Figure 3(a) shows the obtained ΔV_{dc} as a function of d in the range 350–650 nm for various $I_{\text{dc},2}$ (see figure caption). For the parameters we are considering here, the mutual synchronization occurs for $I_{\text{dc},2}$ close to $I_{\text{dc},1}$. In the rest of the work, we consider $I_{\text{dc},2} = -0.10035$ mA [blue squares in Fig. 3(a)], but similar qualitative results are achieved for other curves.

Figure 3(b) shows an example of the time evolution of m_x for the fixed and free MTJs upon application of $I_{\text{dc},1} = -0.09$ mA, $I_{\text{ac},1} = 50$ μ A, $f_{\text{ac},1} = 0.5$ GHz, and $I_{\text{dc},2} = -0.10035$ mA at $d = 450$ nm, where the phase difference is near 180° . However, it is worth pointing out that, for a given set of $I_{\text{dc},1}$, $I_{\text{ac},1}$, and $I_{\text{dc},2}$, the intrinsic phase shift (φ_{dc}) between the ac current and the oscillating magnetization depends on the distance between the MTJs, and it is determined by the dipolar coupling. Therefore, it may be adjusted by tuning these parameters. The inset of Fig. 3(c) compares an example of time-domain traces of magnetoresistance, induced by the oscillations of m_x of the fixed MTJ, and the input ac signal for a distance of $d = 450$ nm. The phase difference between the two signals varies as d changes [see main panel of Fig. 3(c)], while the power remains constant (not shown). Hence, it is the distance-dependent phase shift that is the key ingredient for the change of ΔV_{dc} as a function of distance d . This is advantageous, as the phase offers a robust tool, and it can be easily accessed by measurements.

In Note S3 of the Supplemental Material [32], we discuss micromagnetic simulations performed to verify the effect that nonuniformities in the stray-field distribution, due to the quasiuniform magnetization of the MTJs, may have on the magnetization dynamics. Despite the slightly higher frequencies at which synchronization occurs, we do not observe qualitative differences from the macrospin results.

VI. SPINTRONIC MEMS ACCELEROMETER

A. Results

In modeling the whole magnetic-elastic dynamics, we can consider a range of realistic situations, such as a car crash, screen reorientation, and seismic events. Those excitations are generally characterized by a low-frequency response, ranging from few hertz to kilohertz. For this reason, usually, capacitive MEMS-based accelerometers [12,45,46] are designed to have mechanical resonance frequencies ($f_0 = \omega_0/2\pi$) between 1 and 100 kHz, which allows one to consider the quasistatic response of the oscillator in the process of extracting acceleration. In such a condition, when the mechanical resonance is at least 10 times larger than the external acceleration, the latter can be determined from the equilibrium conditions of the forced harmonic oscillator, $a_{\text{ext}} = \omega_0^2 ds$, where ds is the

displacement. Considering the same substrate technology of current MEMS-based devices, the spintronic MEMS accelerometer can exploit the same approach to extract the acceleration directly from displacement, in our case, d . In particular, here, we assume a total mass of the system, $m_{\text{tot}} = 1$ μ g, and an elastic constant of the spring, $k_{\text{el}} = 1$ kN/m [12,45,46]. This combination of m_{tot} and k_{el} gives a resonance frequency of the system, $f_0 \sim 5$ kHz, that is orders of magnitude lower than the ferromagnetic resonance frequency (GHz range); we also consider a typical damping ratio of $\zeta = b/\sqrt{4k_{\text{el}}m_{\text{tot}}} = 0.75$. With such elastic properties, the distance between the MTJs at equilibrium is 500 nm. This value corresponds to the midpoint of the range in which ΔV_{dc} exhibits a linear dependence with d , as shown previously in Fig. 3(a).

As an example, let us set the fixed MTJ in the injection-locking regime by applying $I_{\text{dc},1} = -0.09$ mA, $I_{\text{ac},1} = 50$ μ A, and $f_{\text{ac},1} = 0.5$ GHz. We also inject a current, $I_{\text{dc},2} = -0.10035$ mA, to generate the self-oscillation in the free MTJ. Figure 4(a) shows the time evolution of distance d for different constant accelerations up to $10g$, where $g = 9.81$ m/s² is the acceleration of gravity. The transient elastic dynamics elapses in less than 0.5 ms, and final displacement d corresponds to the forced harmonic case, $a_{\text{ext}} = \omega_0^2 d$. In addition, we find that the transient of the magnetization dynamics occurs in less than 40 ns (not shown here). This time interval is negligible when compared to the elastic dynamics, and it does not impose limitations on the operability of the proposed device. This direct mapping between acceleration and voltage potentially allows one to simplify the acquisition process, the extra circuitry, and the postprocessing to evaluate acceleration. In other words, to determine the displacement, we exploit its linear effect on the output voltage, ΔV_{dc} , demonstrated in the static case shown in Fig. 3(a) and confirmed from Fig. 4(a). By performing a preliminary calibration of the response of ΔV_{dc} as a function of d , it is possible to translate the measured output voltage into the displacement, and consequently, acceleration a_{ext} .

Once the device is validated for constant accelerations, we consider a more realistic case by mimicking the acceleration and deceleration profile of a car, for instance, to decide whether to issue an attention warning to the driver. The top panel of Fig. 4(b) shows $a_{\text{ext}}(t)$ that we provide as an input to the accelerometer. We employ the same mechanical parameters utilized previously and simulate the response of the system under the external acceleration, $a_{\text{ext}}(t)$, which has a maximum amplitude of $-10g$. With these parameters, the mechanical oscillator adapts to the external acceleration within 0.5 ms; thus a few milliseconds are sufficient to evaluate the performance of the system. The middle and bottom panels of Fig. 4(b) show the time evolution of the relative displacement, d , of the free MTJ with respect to the fixed MTJ and the time trace of ΔV_{dc} generated across the fixed MTJ in

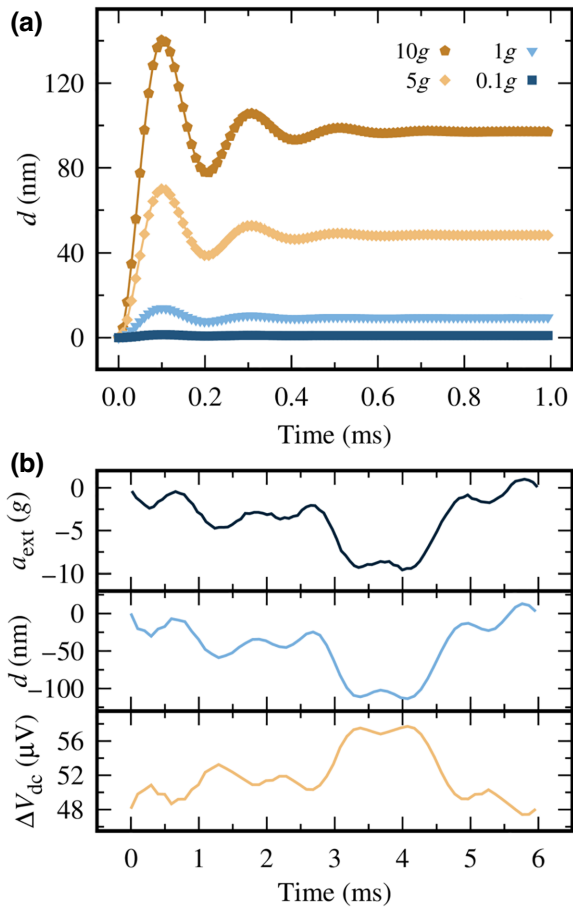


FIG. 4. (a) Displacement of the free MTJ with respect to its initial position as a function of time when the device is subjected to different constant external accelerations, given in units of g . (b) Input time-dependent external acceleration, a_{ext} , given in units of acceleration of gravity, g (top panel); relative displacement, d , of the free MTJ from the fixed MTJ (middle panel); and time-dependent rectification voltage, ΔV_{dc} , measured at the fixed MTJ (bottom panel) in response to a_{ext} .

response to $a_{\text{ext}}(t)$, respectively. From the figure, the linear relationship between d and ΔV_{dc} is evident by inspection: the variation of ΔV_{dc} follows that of d , with the two curves overlapping perfectly once the sign of ΔV_{dc} is changed. In fact, for negative displacements (free MTJ moving closer to the fixed MTJ), ΔV_{dc} is positive, which is clear from Fig. 3(a). We record a variation of ΔV_{dc} on the order of $10 \mu\text{V}$, as expected from the static case and the constant-acceleration test. A comparison of the three panels of Fig. 4(b) shows clearly the direct mapping between ΔV_{dc} , d , and a_{ext} , proving the goodness of the proposed approach. We would like to stress that the simulated timescale is faster than the actual event, in which a_{ext} varies over the range of seconds or longer. The choice is dictated by the computational time required to access such long times, and the results do not exhibit any effect

attributable to excessively fast dynamics. On the contrary, it is clear that, in the case of external accelerations with a lower frequency, the proposed spintronic MEMS device would operate successfully.

In the absence of a whole circuitry evaluation, to estimate the energy consumption of the device due to the injection of dc currents into both MTJs, which is required to exploit the spintronic features of the MTJs, one can extract it from the average MTJ resistance ($R_{\text{MTJ,av}}$). Following the work of Zeng *et al.* [47] on analogous MTJ devices [refer to the current region marked as B1 in Fig. 1(c) of Ref. [47]], $R_{\text{MTJ,av}}$ can be estimated at around 800Ω . Thus, by considering working currents, $I_{\text{dc},\{1,2\}}$, of -0.1 mA , we can estimate a power consumption lower than $20 \mu\text{W}$ by taking into account both the free and fixed MTJs. This estimated power consumption is comparable with or better than those of commercial MEMS-based devices, as reported in data sheets of commercially available accelerometers [48,49].

A. Sensitivity of the spintronic MEMS accelerometer

There are various figures of merit that characterize a sensor, depending on the transduction mechanisms involved [12,46,50]. One of the most common in capacitive MEMS-based accelerometers is the capacitance sensitivity, i.e., the change in capacitance with respect to external acceleration. However, the absence of the capacitive element, which is a specificity of the proposed idea, does not allow us to make a comparison to this figure of merit. On the other hand, we can use a sensitivity defined as the ratio between the amplitude of external acceleration and the readout voltage. Since the variation of ΔV_{dc} is on the order of tens of microvolts, as shown in Figs. 3 and 4, we obtain sensitivities on the order of $0.5 \mu\text{V}/g$, considering directly the voltage extracted across the MTJ without any amplification or postprocessing. We wish to stress that the aim of this work is to present a design that may drive the development of alternative types of devices based on spintronics. Optimization of the device has not been performed at this stage. However, by tuning opportunely the MTJ-setup properties, higher output voltages and higher sensitivities with the spintronic diode effect can be obtained. The displacement or mechanical sensitivity, proportional to $1/\omega_0^2$, relates to the mechanical response of the device, and in capacitive MEMS-based accelerometers, it is related to the displacement of the proof mass along the measurement axis and external acceleration. In our design, we can relate the displacement of the free MTJ with the acceleration by applying different accelerations and extract it as the slope of the linear relationship between the two quantities. Considering the same substrate technology, we obtain a mechanical sensitivity of around $10 \text{ nm}/g$ for the chosen mechanical parameters.

VII. SUMMARY AND CONCLUSIONS

We propose a spintronic MEMS accelerometer based on two MTJs, magnetically and elastically coupled, that are both working as an STNO with bias currents on the order of mA. The oscillatory frequency of the fixed MTJ is controlled by an ac current that drives injection locking to enable the use of the spintronic diode effect as the read-out mechanism of the acceleration applied to the device. We emphasize that the elastic connection between the two substrates on which the MTJs are fabricated can also be realized by exploiting the same technology as that used for capacitive MEMS accelerometers, which makes the proposed device technologically appealing. Moreover, while the intrinsic magnetic coupling between the MTJs is often considered disruptive in applications [51–53], here it plays a crucial role due to its strong dependence on the position. The idea of a spintronic MEMS accelerometer can be scalable to smaller systems and the sensitivity can be enhanced by designing a network of spintronic MEMSs.

Overall, the major potential advantages of the spintronic MEMS accelerometer are the compatibility with current technological implementations of MTJs, a robust and simple reading scheme [20,30], and low power requirements. In fact, the spintronic accelerometer proposed here senses the acceleration directly as voltage variation across the fixed MTJ, in contrast to state-of-the-art integrable MEMS-based devices, where a circuit to convert the capacitance variation into an output voltage is needed. In conclusion, we believe that this idea can be a stimulus for the spintronic community to design experiments and expand the application of MTJs for sensors.

ACKNOWLEDGMENTS

The research was supported by Projects No. PRIN 2020LWPKH7 and No. PRIN 20225YF2S4 funded by the Italian Ministry of University and Research and by the Petaspin Association [54]. The work at the University of Messina was also supported under Project No. 101070287 — SWAN-on-chip — HORIZON-CL4-2021-DIGITAL-EMERGING-01 funded by the European Union. D.R. acknowledges the project PON Ricerca e Innovazione D.M. 10/08/2021 Grant No. 1062. The work at Northwestern University was supported by the National Science Foundation (NSF), Division of Electrical, Communications and Cyber Systems (ECCS), under Grant No. 2203242.

[1] D. S. Eddy and D. R. Sparks, Application of MEMS technology in automotive sensors and actuators, *Proc. IEEE* **86**, 1747 (1998).

- [2] M. Grankin, E. Khavkina, and A. Ometov, in *2012 12th Conference of Open Innovations Association (FRUCT), Vols. 2012-Novem* (IEEE 2012), p. 1.
- [3] A. D’Alessandro, S. Scudero, and G. Vitale, A review of the capacitive MEMS for seismology, *Sensors* **19**, 3093 (2019).
- [4] R. Xu, S. Zhou, and W. J. Li, MEMS accelerometer based nonspecific-user hand gesture recognition, *IEEE Sens. J.* **12**, 1166 (2012).
- [5] D. Gorecky, M. Schmitt, M. Loskyll, and D. Zühlke, in *Proceedings – 2014 12th IEEE International Conference on Industrial Informatics, INDIN 2014* (2014), p. 289.
- [6] H. Sun, M. Yin, W. Wei, J. Li, H. Wang, and X. Jin, MEMS based energy harvesting for the internet of things: A survey, *Microsyst. Technol.* **24**, 2853 (2018).
- [7] M. Masoud, Y. Jaradat, A. Manasrah, and I. Jannoud, Sensors of smart devices in the internet of everything (IoE) era: Big opportunities and massive doubts, *J. Sens.* **2019**, 1 (2019).
- [8] S. Fu, Z. Wan, W. Lu, H. Liu, P. Zhang, B. Yu, J. Tan, F. Pan, and Z. Liu, High-accuracy virtual testing of air conditioner’s digital twin focusing on key material’s deformation and fracture behavior prediction, *Sci. Rep.* **12**, 12432 (2022).
- [9] J. W. Judy, Microelectromechanical systems (MEMS): Fabrication, design and applications, *Smart Mater. Struct.* **10**, 1115 (2001).
- [10] Peng Qu, Hongwei Qu, S. Gollapudi, R. Bidthanapally, and G. Srinivasan, in *2015 IEEE SENSORS* (IEEE, 2015), p. 1.
- [11] Y. Zhai, H. Li, Z. Tao, X. Cao, C. Yang, Z. Che, and T. Xu, Design, fabrication and test of a bulk SiC MEMS accelerometer, *Microelectron. Eng.* **260**, 111793 (2022).
- [12] M. Benmessaoud and M. M. Nasreddine, Optimization of MEMS capacitive accelerometer, *Microsyst. Technol.* **19**, 713 (2013).
- [13] M. Varanis, A. Silva, A. Mereles, and R. Pederiva, MEMS accelerometers for mechanical vibrations analysis: A comprehensive review with applications, *J. Braz. Soc. Mech. Sci. Eng.* **40**, 1 (2018).
- [14] STT-MRAM: Introduction and Market Status, (unpublished).
- [15] B. Jinnai, K. Watanabe, S. Fukami, and H. Ohno, Scaling magnetic tunnel junction down to single-digit nanometers—challenges and prospects, *Appl. Phys. Lett.* **116**, 160501 (2020).
- [16] N. Maciel, E. Marques, L. Naviner, Y. Zhou, and H. Cai, Magnetic tunnel junction applications, *Sensors (Switzerland)* **20**, 1 (2020).
- [17] Z. Q. Lei, G. J. Li, W. F. Egelhoff, P. T. Lai, and P. W. T. Pong, Review of noise sources in magnetic tunnel junction sensors, *IEEE Trans. Magn.* **47**, 602 (2011).
- [18] Z. M. Zeng, P. Khalili Amiri, J. A. Katine, J. Langer, K. L. Wang, and H. W. Jiang, Nanoscale magnetic tunnel junction sensors with perpendicular anisotropy sensing layer, *Appl. Phys. Lett.* **101**, 062412 (2012).
- [19] A. Hirohata, K. Yamada, Y. Nakatani, I.-L. Prejbeanu, B. Diény, P. Pirro, and B. Hillebrands, Review on spintronics: Principles and device applications, *J. Magn. Magn. Mater.* **509**, 166711 (2020).
- [20] G. Finocchio, R. Tomasello, B. Fang, A. Giordano, V. Puliafito, M. Carpentieri, and Z. Zeng, Perspectives

- on spintronic diodes, *Appl. Phys. Lett.* **118**, 160502 (2021).
- [21] M. A. Khan, J. Sun, B. Li, A. Przybysz, and J. Kosel, Magnetic sensors—a review and recent technologies, *Eng. Res. Express* **3**, 022005 (2021).
- [22] B. Fang, M. Carpentieri, S. Louis, V. Tiberkevich, A. Slavin, I. N. Krivorotov, R. Tomasello, A. Giordano, H. Jiang, J. Cai, *et al.*, Experimental Demonstration of Spintronic Broadband Microwave Detectors and Their Capability for Powering Nanodevices, *Phys. Rev. Appl.* **11**, 014022 (2019).
- [23] S. Bhatti, R. Sbiaa, A. Hirohata, H. Ohno, S. Fukami, and S. N. Piramanayagam, Spintronics based random access memory: A review, *Mater. Today* **20**, 530 (2017).
- [24] Z. Zeng, G. Finocchio, and H. Jiang, Spin transfer nano-oscillators, *Nanoscale* **5**, 2219 (2013).
- [25] R. R. Katti, Accelerometer Using Magnetic Tunnel Junction, US11150312B2 (2021).
- [26] R. R. Katti, Magnetic Spin Hall Effect Spintronic Accelerometer, US11054438B2 (2021).
- [27] R. R. Katti, Spintronic Accelerometer, EP3623820A1 (2020).
- [28] R. R. Katti, Spintronic Gyroscopic Sensor Device, EP3623757A1 (2020).
- [29] R. R. Katti and E. F. Ambrose, Spintronic Mechanical Shock And Vibration Sensor Device, EP3623777A1 (2020).
- [30] A. A. Tulapurkar, Y. Suzuki, A. Fukushima, H. Kubota, H. Maehara, K. Tsunekawa, D. D. Djayaprawira, N. Watanabe, and S. Yuasa, Spin-torque diode effect in magnetic tunnel junctions, *Nature* **438**, 339 (2005).
- [31] M. Quinsat, J. F. Sierra, I. Firastrau, V. Tiberkevich, A. Slavin, D. Gusakova, L. D. Buda-Prejbeanu, M. Zarudniev, J.-P. Michel, U. Ebels, *et al.*, Injection locking of tunnel junction oscillators to a microwave current, *Appl. Phys. Lett.* **98**, 182503 (2011).
- [32] See the Supplemental Material at <http://link.aps.org/supplemental/10.1103/PhysRevApplied.20.034003> for an alternative working principle, an evaluation of the macrospin hypothesis, and the micromagnetic verification of mutual synchronization between MTJs.
- [33] Y.-M. Lin, Micro-Electro-Mechanical Systems (Mems) Capacitive Sensing Circuit, US8023667B2 (2011).
- [34] S. Long, Y. Liu, K. He, X. Tang, and Q. Chen, 116 dB dynamic range CMOS readout circuit for MEMS capacitive accelerometer, *J. Semicond.* **35**, 095004 (2014).
- [35] J. C. Slonczewski, Current-driven excitation of magnetic multilayers, *J. Magn. Magn. Mater.* **159**, L1 (1996).
- [36] A. Meo, C. E. Cronshaw, S. Jenkins, A. Lees, and R. F. L. Evans, Spin-transfer and spin-orbit torques in the Landau–Lifshitz–Gilbert equation, *J. Phys.: Condens. Matter* **51**, 025801 (2022).
- [37] A. Giordano, G. Finocchio, L. Torres, M. Carpentieri, and B. Azzerboni, Semi-implicit integration scheme for Landau-Lifshitz-Gilbert-Slonczewski equation, *J. Appl. Phys.* **111**, 7 (2012).
- [38] J. C. Slonczewski, Currents, torques, and polarization factors in magnetic tunnel junctions, *Phys. Rev. B* **71**, 024411 (2005).
- [39] G. Finocchio, B. Azzerboni, G. D. Fuchs, R. A. Buhrman, and L. Torres, Micromagnetic modeling of magnetization switching driven by spin-polarized current in magnetic tunnel junctions, *J. Appl. Phys.* **101**, 063914 (2007).
- [40] B. Fang, M. Carpentieri, X. Hao, H. Jiang, J. A. Katine, I. N. Krivorotov, B. Ocker, J. Langer, K. L. Wang, B. Zhang, *et al.*, Giant spin-torque diode sensitivity in the absence of bias magnetic field, *Nat. Commun.* **7**, 11259 (2016).
- [41] L. Mazza, V. Puliafito, E. Raimondo, A. Giordano, Z. Zeng, M. Carpentieri, and G. Finocchio, Computing with Injection-Locked Spintronic Diodes, *Phys. Rev. Appl.* **17**, 014045 (2022).
- [42] T. H. Boyer, The force on a magnetic dipole, *Am. J. Phys.* **56**, 688 (1988).
- [43] A. Slavin and V. Tiberkevich, Nonlinear auto-oscillator theory of microwave generation by spin-polarized current, *IEEE Trans. Magn.* **45**, 1875 (2009).
- [44] N. Locatelli, A. Hamadeh, F. A. Araujo, A. D. Belanovsky, P. N. Skirdkov, R. Lebrun, V. V. Naletov, K. A. Zvezdin, M. Muñoz, J. Grollier, *et al.*, Efficient synchronization of dipolarly coupled vortex-based spin transfer nano-oscillators, *Sci. Rep.* **5**, 17039 (2015).
- [45] M. Keshavarzi and J. Yavand Hasani, Design and optimization of fully differential capacitive MEMS accelerometer based on surface micromachining, *Microsyst. Technol.* **25**, 1369 (2019).
- [46] L. Lutiani-Silva, J. R. Rodrigues, A. Passaro, and V. R. Almeida, MEMS capacitive accelerometer: Dynamic sensitivity analysis based on analytical squeeze film damping and mechanical thermoelasticity approaches, *SN Appl. Sci.* **1**, 1 (2019).
- [47] Z. Zeng, G. Finocchio, B. Zhang, P. Khalili Amiri, J. A. Katine, I. N. Krivorotov, Y. Huai, J. Langer, B. Azzerboni, K. L. Wang, and H. Jiang, Ultralow-current-density and bias-field-free spin-transfer nano-oscillator, *Sci. Rep.* **3**, 1426 (2013).
- [48] STMicroelectronics Accelerometers Catalogue, <https://www.st.com/en/mems-and-sensors/accelerometers.html>
- [49] Bosch Accelerometer Catalogue, <https://www.bosch-sensortec.com/products/motion-sensors/accelerometers/>
- [50] A. Dwivedi, P. Asthana, G. Khanna, and T. Chaudhary, in *Hearing Loss – From Multidisciplinary Teamwork to Public Health* (IntechOpen, 2021).
- [51] Y. H. Wang, S. H. Huang, D. Y. Wang, K. H. Shen, C. W. Chien, K. M. Kuo, S. Y. Yang, and D. L. Deng, in *Technical Digest – International Electron Devices Meeting, IEDM*, edited by T.-C. Wang (2012).
- [52] S. Jenkins, A. Meo, L. E. Elliott, S. K. Piotrowski, M. Bapna, R. W. Chantrell, S. A. Majetich, and R. F. L. Evans, Magnetic stray fields in nanoscale magnetic tunnel junctions, *J. Phys. D: Appl. Phys.* **53**, 044001 (2020).
- [53] S. Ohuchida, K. Ito, M. Muraguchi, and T. Endoh, 10 nm P-MTJ Array Design for Suppressing Switching Delay Induced by Interference Due to Magnetic Dipole Interaction for High Density STT-MRAM, (2018).
- [54] <https://www.petaspin.com/>.